Atmos. Meas. Tech. Discuss., 6, 4279–4312, 2013
www.atmos-meas-tech-discuss.net/6/4279/2013/
doi:10.5194/amtd-6-4279-2013

Atmospheric Measurement Techniques Discussions
Open Access

Validation of satellite OPEMW precipitation product with ground-based weather radar and rain gauge networks

D. Cimini[1,2], F. Romano[1], E. Ricciardelli[1], F. Di Paola[1], M. Viggiano[1], F. S. Marzano[2,3], V. Colaiuda[2], E. Picciotti[4], G. Vulpiani[5], and V. Cuomo[1]

[1]IMAA-CNR, C. da S. Loja, Tito Scalo, 85050, Potenza, Italy
[2]CETEMPS, University of L'Aquila, Via Vetoio 1, 67100, L'Aquila, Italy
[3]DIET, University of Rome La Sapienza, Via Eudossiana 18, 00184, Roma, Italy
[4]HIMET s.r.l., Strada Statale 17 OVEST, 36, 67100, L'Aquila, Italy
[5]Department of Civil Protection, Via Vitorchiano 2, 00189 Rome, Italy

Received: 22 February 2013 – Accepted: 22 April 2013 – Published: 14 May 2013

Correspondence to: D. Cimini (cimini@imaa.cnr.it)

Published by Copernicus Publications on behalf of the European Geosciences Union.

Abstract

The Precipitation Estimation at Microwave Frequencies (PEMW) algorithm was developed at the Institute of Methodologies for Environmental Analysis of the National Research Council of Italy (IMAA-CNR) for inferring surface rain intensity (sri) from satellite passive microwave observations in the range from 89 to 190 GHz. The operational version of PEMW (OPEMW) has been running continuously at IMAA-CNR for two years, producing sri estimates feeding an operational hydrological model for forecasting flood alerts. This paper presents the validation of OPEMW against simultaneous ground-based observations obtained by a network of 20 weather radars and a network of more than 3000 rain gauges distributed over the Italian peninsula and main islands. The validation effort uses a data set spanning a one-year period (July 2011–June 2012). The effort evaluates dichotomous and continuous scores for the assessment of rain detection and quantitative estimate, respectively, investigating both spatial and temporal features. The analysis demonstrates 98 % accuracy in correctly identifying rainy and non-rainy areas, and it quantifies the increased ability (with respect to random chance) to detect rainy and non-rainy areas (0.42–0.45 Heidke skill score) or rainy areas only (0.27–0.29 equitable threat score). Performances are better than average during summer, fall, and spring, while worse than average in the winter season. The spatial-temporal analysis does not show seasonal dependence except for larger mean absolute difference over the Alps and northern Apennines during winter, attributable to residual effect of snow cover. A binned analysis in the 0–15 $\mathrm{mm\,h^{-1}}$ range suggests that OPEMW tends to slightly overestimate sri values below 6–7 $\mathrm{mm\,h^{-1}}$, and to underestimate sri above those values. Depending upon the ground reference (either rain gauges or weather radars), the mean difference is 0.8–2.8 $\mathrm{mm\,h^{-1}}$, with a standard deviation within 2.6–3.1 $\mathrm{mm\,h^{-1}}$ and correlation coefficient within 0.8–0.9. The monthly mean difference was shown to remain within $\pm 1\,\mathrm{mm\,h^{-1}}$ with respect to rain gauges and within $-2\,\mathrm{mm\,h^{-1}}$ with respect to weather radars, with 2–4 $\mathrm{mm\,h^{-1}}$ standard deviation.

AMTD
6, 4279–4312, 2013

1 Introduction

The accurate estimation of rainfall is crucial for many applications, including its short-term assessment and long-term monitoring. A comprehensive overview of recent activities, ongoing research, and future plans about precipitation remote sensing and its applications is given by Levizzani et al. (2010). Rainfall estimation algorithms, validation strategies, precipitation modeling, and assimilation into numerical weather prediction and hydrological high-resolution models are topics still under investigation, especially over land (e.g. Anagnostou, 2004). The likely increase of extreme events due to climate-related forcing brings even more importance to rainfall retrieval as a means for monitoring environmental hazards (e.g. Nunes and Roads, 2007). The assessment of precipitation detection and quantitative estimation from space remains a major issue (e.g. Ebert et al., 2007). In the last decades several retrieval algorithms have been developed based on the exploitation of microwave and millimetre-wave spaceborne radiometers aboard low Earth orbit (LEO) satellites (e.g. Kidd and Levizzani, 2011). Among these, a number of approaches have been proposed by the Institute of Methodologies for the Environmental Analysis of the National Research Council of Italy (IMAA-CNR) to retrieve cloud and rainfall information from satellite observations (Romano et al., 2007; Ricciardelli et al., 2008, 2010; Di Tomaso et al., 2009). In particular, the Precipitation Estimation at Microwave Frequencies (PEMW) algorithm was developed to infer rain rates from satellite passive microwave observations in the 89 to 190 GHz range (Di Tomaso et al., 2009). The PEMW algorithm relies on satellite observations made by the Advanced Microwave Sounding Unit/B (AMSU/B) or the Microwave Humidity Sounder (MHS) on board the US National Oceanic and Atmospheric Administration (NOAA) satellites and/or the European Polar Satellite MetOp-A. The PEMW performances were tested (Di Tomaso et al., 2009) at relative high latitudes using data from the UK NIMROD radar network and at low latitudes using rain gauges on the island of Nauru in the tropical western Pacific, belonging to the US Atmospheric Radiation Measurement (ARM) program. A total of 6 case studies were

AMTD
6, 4279–4312, 2013

used for the validation of the PEMW algorithm against the NIMROD radar observations, while less than 30 satellite overpasses were used for the validation against the one-point rain gauge measurements in Nauru. Since then, the operational version of PEMW (OPEMW) has been running at IMAA-CNR in support to numerical hydrometeorology and flood-hazard-alert systems. However, the validation of OPEMW over the geographical area where its estimates are actually utilized – i.e. the Italian territory – has never been tested before. Thus, similarly to what has been proposed previously by Antonelli et al. (2010), this analysis carries out a detailed validation of the OPEMW product by comparing against the weather radar network and the rain gauge network deployed over the Italian territory.

This paper is organized as the following: Sect. 2 describes the data set under consideration; Sect. 3 summarizes the methodology used for data comparison; Sect. 4 reports the results of the data analysis; and Sect. 5 summarises the quantitative results and draws the final conclusions.

2 Data set

2.1 OPEMW

OPEMW is the software package developed at IMAA-CNR that implements and runs operationally the PEMW algorithm. OPEMW has been running at IMAA-CNR since 2010 in support to numerical hydrometeorology and flood-hazard-alert systems. The details of PEMW are described in Di Tomaso et al. (2009). PEMW was developed to work with observations from AMSU/B, flying aboard the NOAA Polar Operational Environmental Satellites (POES). PEMW was later adapted to work with observations from MHS, flying aboard the most recent NOAA POES satellites and the European Polar System (EPS) MetOp-A belonging to the European Organisation for the Exploitation of Meteorological Satellites (EUMETSAT). POES and EPS are respectively the US and European contributions to the Initial Joint Polar-Orbiting Operational Satellite System

AMTD
6, 4279–4312, 2013

(IJPS). Here we just remind that both AMSU-B and MHS are cross-track, line scanning microwave radiometers measuring radiances in five channels in the frequency range from 89 to 190 GHz. AMSU-B and MHS exploit similar channels: center frequencies for the AMSU-B channels are 89, 150, 183±1, 183±3, and 183±7 GHz; while for the MHS channels are 89, 157, 183 ± 1, 183 ± 3, and 190 GHz. Therefore, the two instruments differ just at channel number 2 (150 vs. 157 GHz) and 5 (183±7 vs. 190 GHz); however, the differences are more technical rather than functional, and the two channel duplets show the same fundamental features. AMSU-B and MHS fly at a nominal altitude of 850 km and they observe the Earth scanning circa ±50° across nadir, taking 90 consecutive fields-of-view (FOVs) per scan. The five channels are co-registered with 1.1° antenna beam width. At nadir, the antenna footprint corresponds to a circle of diameter approximately 16 km. Due to the cross-track observation geometry, away from nadir the FOVs have an ellipsoidal shape. The FOV axes range from 16 by 16 km at nadir to 51 by 25 km at maximum scanning angle (Bennartz, 2000), the first axis being for the cross-track and the second for the along-track direction. Further details on the instruments features can be found in the NOAA KLM user's guide (NCDC/NOAA, 2008) and the ATOVS Level 1b Product Guide (EUMETSAT, 2010). At the time of writing there are five operational NOAA POES satellites (namely the N-15, N-16, N-17, N-18, and N-19) spaced approximately 2–6 h apart and carrying either the AMSU-B (N-15, N-16, and N-17) or the MHS (N-18 and N-19) instruments; in addition, there are two operational EPS satellites, MetOp-A and MetOp-B, both carrying the MHS instrument.

The AMSU-B and MHS raw data are received in near-real time at IMAA-CNR and processed with the AAPP code (UK Met Office, 2011). The level 1c data are then processed by OPEMW, and the rain rate product is sent to the Centre of Excellence for the integration of remote sensing and modelling for the prediction of severe weather (CETEMPS) and also stored in the IMAA-CNR archive. The present version (V4) of OPEMW has been running since May 2011. The data set considered here covers one full year, from July 2011 to June 2012. For this period the three AMSU-B instruments were unavailable due to instrumental failures, and the MetOp-B was still in its

AMTD
6, 4279–4312, 2013

pre-launch and commissioning phases; thus the following analysis focuses on MHS observations from N-18, N-19, and MetOp-A. An example of the surface rain intensity (sri, $mm\,h^{-1}$) map product by OPEMW is shown in Fig. 1.

2.2 Weather radar network

Microwave weather radars are considered a fairly established technique for retrieving rain rate fields over large areas from measured reflectivity volumes. In the framework of the national early-warning system for multi-risks management, the Italian Department of Civil Protection (DPC) was appointed to complement the existing weather radar systems in order to increase the coverage of the Italian territory. The resulting Italian national weather radar network is coordinated by the DPC, in collaboration with regional authorities, research centres, the Air Traffic Control service (ENAV), and the Meteorological Service of the Air Force (CNMCA). Once completed, the Italian radar network shall include twenty-five C-band (~ 5 GHz) radars (including seven polarimetric systems) and five dual-polarized X-band (~ 10 GHz) radars, deployed throughout the country (Vulpiani et al., 2008a). Currently, the radar network is composed by twenty weather radars: ten C-band radars belonging to regional authorities (five of which are polarimetric), two C-band radars owned by ENAV, and six C-band radars (two of which are polarimetric) plus two X-band polarimetric radars owned directly by the DPC. The DPC collects radar data in near real-time by satellite links to the two national Radar Primary Centres (RPC), one located at the DPC headquarter in Rome and the other at the Centro Internazionale in Monitoraggio Ambientale (CIMA) Research Foundation in Savona. Procedures for mitigating ground clutter, anomalous propagation, beam blockage effects are applied (Vulpiani et al., 2008a). The radar volumes are then centrally processed to produce the so-called radar network composite (RNC) of products such as the Vertical Maximum Intensity (VMI, dBZ), the Constant Altitude Plan Position Indicator (CAPPI, dBZ), the surface rain intensity (sri, $mm\,h^{-1}$), and the one-hour accumulated surface rain total (srt, mm). All products are obtained over a grid of 1400 by 1400 km^2 with spatial resolution of ~ 1 km and temporal resolution of 15 min; the

AMTD
6, 4279–4312, 2013

gridded products are then distributed to the hydrological and meteorological regional services. The RNC sri product, used here, represents the best radar estimate available for the period under analysis. It must be underlined that this was not adjusted to match rain gauge products, even though statistical techniques are under testing (Marzano et al., 2012). Procedures to improve the quality of the RNC sri product, including attenuation compensation, polarimetric rainfall inversion techniques, and adaptive algorithms to retrieve mean vertical profiles of reflectivity (VPR) are currently under validation at DPC (Vulpiani et al., 2008a, 2012). An example of the RNC sri product is shown in Fig. 2, for the same time interval of Fig. 1.

2.3 Rain gauge network

Several rain gauge networks have been deployed over the Italian territory through the years, belonging to independent regional and national authorities. More recently, DPC was appointed to manage the existing rain gauge networks in collaboration with other regional and national authorities. This integrated network is one of the densest in the world, with more than 3000 rain gauges (Vulpiani et al., 2012). Figure 3 shows the distribution of the rain gauges over Italy. Rain gauge data acquisition and processing are performed by regional authorities at different temporal intervals, ranging from 5 to 30 min. Typically some 65–85 % of the total number of rain gauges is available at the same time. The rain gauge network (RGN) data are collected and centrally processed in near-real time by the DPC. The set of 1 h accumulated rain for each rain gauge of the network represents the RGN surface rain intensity (sri, $mm\,h^{-1}$) product. The DPC distributes the RGN sri product through DEWETRA, a web-based software developed by CIMA Research Foundation on behalf of the DPC. Figure 3 also shows the RGN sri, color-coded according to accumulated rain thresholds (referred to the last 24 h), for the same 1 h period containing the satellite overpass in Fig. 1 and the radar composite in Fig. 2.

AMTD
6, 4279–4312, 2013

3 Methodology

The OPEMW sri product is validated against the sri products from the radar composite network (RNC) and the rain gauge network (RGN). The data set considered here covers one full year (July 2011–June 2012); data were processed for searching space-time colocation, ensuring data quality, and finally computing statistical scores for quantitative performance evaluation.

3.1 Space-time colocation

The OPEMW surface rain intensity product is colocated with the ground-based products so that each satellite FOV is associated with the corresponding surface rain intensity values derived from RNC and RGN.

The temporal colocation is obtained as follows:

- Each OPEMW sri product is associated to the time of the satellite overpass, since it is a nearly instantaneous observation.
- Then, the procedure searches for a RNC sri product within 8 min before/after the satellite overpass, which is usually found since the RNC sri product is available every 15 min.
- Finally, the procedure searches for the RGN sri product corresponding to the 1 h time window in which the satellite overpass has occurred. Note that, differently from OPEMW and RNC sri products, the RGN sri product is not a nearly-instantaneous observation, because it is computed as the hourly accumulated rainfall.

The spatial colocation is obtained by convoluting either the RNC or RGN sri products to the MHS FOVs, taking into account the antenna pattern, assumed as Gaussian, and the ellipsoidal shape at different viewing angles (Bennartz, 2000). For each FOV, the convolution usually takes some 200–1000 RNC pixels and some 5–180 rain gauges.

AMTD
6, 4279–4312, 2013

Thus, the colocation procedure typically smoothes down high sri values that may happen at some RNC pixels or RGN sites with the surrounding lower values.

3.2 Data quality

The single FOV estimate is in general prone to geolocation and co-location errors. In fact, satellite observations suffer from considerable geolocation errors. Errors up to two pixels can be in both the along and the cross-track direction, leading to considerable geographical misplacement. Moreover, additional geolocation uncertainty stems from the parallax error. This error increases proportionally with increasing observation angle and altitude of the cloud melting layer and it can contribute with up to 10 km to the misplacement of raining areas (Antonelli et al., 2010). Additional uncertainty is related to the spatial heterogeneity, the so called beam-filling problem (Kummerow, 1998), which refers to the fact that the observed precipitating area does not fill the satellite FOV homogeneously due to spatial variability in the sub-FOV scale. Finally, sources of inconsistencies between satellite and ground based observations may be related to erroneous measurements.

Therefore, measures for data quality control are applied during the spatial colocation procedure. Geolocation errors are mitigated according to the platform during the production of level 1c data. In order to prevent unrealistic sri values entering in the statistical analysis, the procedure discards RGN sri values higher than 150 $mm\,h^{-1}$, assumed to be the upper limit for 1 h accumulated precipitation. The same upper limitation is adopted for the instantaneous RNC sri values. To minimize the inconsistency related to beam-filling issues, the procedure discards the FOVs covered by less than 3/4 by RNC pixels, and it considers only those FOVs for which 95 % of the pixels are either clear or covered by rain (i.e. leaving 5 % tolerance with respect to considering completely clear or fully covered FOVs only). Similarly, FOVs with less than 10 rain gauges are discarded, and only those for which more than 95 % of the rain gauge detects either rain or not rain are considered.

AMTD
6, 4279–4312, 2013

3.3 Statistical scores

The validation of the OPEMW sri product against the ground-based RNC and RGN reference products is performed through the assessment of a number of statistical scores. Here we present both dichotomous and continuous scores, used to assess quantitatively the accuracy of rain detection and estimation, respectively.

The dichotomous scores, used for the assessment of rain detection accuracy, are based on the contingency table; the contingency table reports the hits, misses, correct negatives, and false alarms of OPEMW rain detection (0/1 for rainy/non-rainy) with respect to RNC and RGN sri. The dichotomous scores include the accuracy, the frequency bias (FB) score, the probability of detection (POD), the false alarm ratio (FAR), the Heidke skill score (HSS), and finally the equitable threat score (ETS). Equations for these scores are given in the Appendix A. The accuracy score indicates the fraction of all the FOVs that have been correctly identified as rainy or non-rainy; however, the high occurrence of non-rainy FOVs strongly influences this accuracy score. Similarly to this, the HSS indicates the fraction of correctly identified FOVs (as rainy or non-rainy), but after eliminating the fraction correctly identified due to random chance. Even more stringent, the ETS indicates the fraction of correctly identified FOVs as rainy after eliminating the fraction due to random chance. The FB score indicates whether there is a tendency to over or underestimate the area subject to rain (bias score > 1 or < 1, respectively). Finally, the POD quantifies the ability to detect the rainy FOVs only, while the FAR provides a measure for the fraction of non-rainy FOVs that have been erroneously detected as rainy.

The continuous scores, used for the assessment of sri estimation accuracy, are applied to the data set after the "binning", following the approach introduced by Ferraro and Marks (1995). In this approach the reference data (RNC and RGN) are binned in $1\,\mathrm{mm\,h^{-1}}$ sri intervals and the corresponding satellite estimates are averaged and associated to each bin. The binned analysis is extremely useful, as it minimizes match-up errors between ground and satellite observations and it ensures equal emphasis on the

AMTD
6, 4279–4312, 2013

entire range of sri. The dataset after the binning is used to compute the mean (AVG), standard deviation (STD), and root-mean squared (RMS) difference, the correlation coefficient (COR), and the slope (SLP) and intercept (INT) of a linear fit. Finally, the mean and standard deviation difference of the original data set (before binning) have been used to quantify the single FOV estimate accuracy.

4 Results

The results of the validation of the OPEMW sri product against the ground-based RNC and RGN reference products are presented for the one-year data set under consideration (July 2011–June 2012). Figure 4 presents the histograms of OPEMW, RGN, and RNC sri products for the full data set, after the colocation procedure, in the 0–16 $mm\,h^{-1}$ range (values greater than 15 $mm\,h^{-1}$ are grouped in the last bin). The distributions of the three sri sources look quite similar, except that OPEMW shows more cases at small values (sri $\sim$ 1 $mm\,h^{-1}$) and fewer cases at large values (sri $\geq$ 15 $mm\,h^{-1}$) relatively to the other two sources.

The following sections report the results of the dichotomous statistical assessment, the continuous statistical assessment, and a spatial and temporal analysis.

4.1 Dichotomous statistical assessment

The dichotomous statistical assessment was performed over the whole data set, containing more than 650 000 OPEMW-RGN match-ups and more than 1 600 000 OPEMW-RNC match-ups. We assume a detection limit of 0.5 $mm\,h^{-1}$, which means that sri values smaller than this limit are set to zero. The overall results are reported in Table 1, also divided into four seasons: Summer (July–September 2011), Fall (October–December 2011), Winter (January–March 2012), and Spring (April–June 2012). Considering all data, the accuracy score shows that OPEMW correctly identifies as rainy or non-rainy most of the FOVs (98 % for both RGN and RNC). However,

AMTD
6, 4279–4312, 2013

the accuracy score is heavily influenced by the high occurrence of non-rainy FOVs (96 % and 98 % for RGN and RNC, respectively), as previously anticipated. The fraction of correct detection after eliminating the portion due purely to random chance is given by the HHS and ETS scores, respectively considering or not the corrected null detection (no rain). The perfect value for HHS and ETS is 1.0 while here these get to HHS = 0.42–0.45 and ETS = 0.27–0.29 (the first number being with respect to RGN while the second to RNC). The FB score is fairly close to unity, its perfect value, although a bit larger with respect to both RGN and RNC, indicating that OPEMW has a tendency to slightly overestimate the precipitating areas. As a consequence, the FAR is rather high (64 %), while the POD is within 55–60 % (for RGN and RNC, respectively). Table 1 also reports the dichotomous scores computed by breaking the data set into the four season introduced above, thus providing information on the seasonal behaviour of the OPEMW performances. All the scores indicate that performances better than the annual average are found for summer, fall, and spring, while significantly worse than average for the winter season. In particular, the low values for POD and HSS together with the high values for FAR and FB seem to suggest that OPEMW tends to overestimate the precipitating areas during winter.

Note that the quantitative values of the above scores depend upon the assumed sri detection limit. For example, Fig. 5 shows the monthly-mean POD as computed using three detection limits, either 0.5, 1.0, and 5.0 $\mathrm{mm\,h^{-1}}$. Figure 5 confirms the seasonal behavior of OPEMW estimates and the performance degradation during the winter season (with respect to both RGN and RNC). The behaviour however becomes less evident as the detection limit increases. Finally, considering the whole data set, the POD gets to 60–66 % (for RGN and RNC, respectively) with a sri threshold of 1 $\mathrm{mm\,h^{-1}}$, while to 83–88 % (for RNC and RGN, respectively) with a sri threshold of 5 $\mathrm{mm\,h^{-1}}$. This demonstrates the increasing OPEMW detection skills as the rainfall becomes more and more significant.

AMTD
6, 4279–4312, 2013

4.2 Continuous statistical assessment

As already mentioned, the continuous statistical assessment was applied to the data set after the "binning", following the approach in Ferraro and Marks (1995). The data sets in Fig. 4 have been processed such that the reference data, either RNC or RGN sri products, are binned in 1 mm h^{-1} sri intervals, and the corresponding satellite estimates are averaged for each bin and the averaged OPEMW sri value is associated to that bin. The results of the binning are shown in Fig. 6 in terms of percentage histograms, i.e. the percentage of all data that fell in each bin. Clearly, considering all the match-up data, including non-raining FOVs, a large portion ($\sim$ 60 %) falls in the first bin. Conversely, a more balanced histogram is obtained when considering only the hits (raining pixels correctly detected), though the number of satellite estimates falling into bins corresponding to increasingly higher sri values decreases drastically. Accordingly, the binning analysis is less and less reliable as the sri value increases and the number of available satellite estimates decreases. In particular, we limited the analysis to bins with a number of satellite estimates larger than 5, causing the sri range to be bound in the 0–15 mm h^{-1} range. Thus, the results of the binning analysis are shown in Fig. 7, where we compare OPEMW sri estimates against both RGN and RNC for the entire year under consideration. The results are presented considering all data and hits only, corresponding to the histograms in Fig. 6. The binned scatter plots show a reasonably good correlation between OPEMW and RGN/RNC sri products, though it is noticeable that OPEMW tends to slightly overestimate lower sri values, and conversely, to underestimate larger sri, with a sort of hinge point roughly around 6–7 mm h^{-1}. Up to 7 mm h^{-1} OPEMW is well correlated with the ground reference, specially with RGN, while the scatter increases significantly for sri >10 mm h^{-1}, likely due to the low number of cases (as seen in Fig. 6). Overall, the mean difference is within 0.8–2.8 mm h^{-1}, the std is within 2.6–3.1 mm h^{-1}, while the correlation is within 0.8–0.9. Better agreement (in terms of rms) is found with RNC than RGN, while the bias for both RGN and RNC is lower when considering hits only, though the above results are strongly influenced

AMTD
6, 4279–4312, 2013

by the larger sri values, which again are less reliable due to much lower statistical significance.

The same analysis, but dividing the dataset into the four seasons introduced earlier, is repeated in Figs. 8 and 9, respectively with respect to RGN and RNC. In Fig. 8 we see that OPEMW agrees quite well with RGN in summer, winter and spring, showing mean difference within 0.9 mm h^{-1}, std within 1.2 mm h^{-1}, rms within 1.3 mm h^{-1}, and correlation greater than 0.9. However, the range of valid sri is limited to less than 10 mm h^{-1} by the low occurrence of higher sri values. The results for the fall season resemble those for the whole year in Fig. 7. Similarly, Fig. 9 shows results with respect to RCN. Here we do not notice significant difference between the four seasons, all of which tend to confirm the results in Fig. 7. Note however that OPEMW tends to overestimate small sri values with respect to RNC (Fig. 9), but not so much with respect to RGN (Fig. 8). This is mainly due to an underestimation of the sri field by RNC related to the complex orography of the Italian territory that causes, apart from significant ground clutter, a range-dependent underestimation due to beam divergence and altitude (Marzano et al., 2004). Mitigation measures are currently under testing at DPC, but are not applied to the current version of RNC.

4.3 Spatial-temporal assessment

The spatial and temporal distribution of the retrieval uncertainties are also important to characterize the OPEMW performances, especially over a territory with complex orography and large seasonal variability such as Italy. To investigate this, we have divided the geographical area in Figs. 1–3 into a 14° by 14° longitude–latitude grid with 0.1° step and computed for each pixel the mean absolute difference between OPEMW and ground-reference (either RGN or RNC) sri products for each of the four seasons introduced above. The results are shown in Figs. 10 and 11, respectively with RGN and RNC as reference. Figures 10 and 11 do not seem to show any particular geographical-seasonal effect, except for an increase in mean absolute difference over the Alps and along the northern Apennines during winter. This effect may be related to the presence

AMTD
6, 4279–4312, 2013

of snow on the ground, which is a well-know source of uncertainty for passive microwave estimates of rainfall. As described in Di Tomaso et al. (2009) the PEMW algorithm applies methods to avoid snow on the ground to be detected as rainfall, based on the observations from the channels less sensitive to ground emissivity. The effects of these methods were shown by Di Tomaso et al. (2009), concluding that the number of false alarms is reduced considerably, but not completely set to zero. Therefore, we believe the increase in mean absolute difference over the main mountain ridges to be a residual effect due to snow on the ground; this seems to be supported also by Table 1 and Fig. 4, showing increasing FAR and decreasing POD during winter.

In Fig. 10 we also notice larger mean absolute difference values over Sicily than for the rest of Italy. This is more evident during winter, but it seems to be present during the other seasons as well. Since there is no hint of this feature in Fig. 11, we argue this may be not related to inaccurate satellite estimates but rather to larger uncertainties affecting the rain gauge network deployed in that region.

Finally, in order to quantify the accuracy of the single FOV estimate and to detect its seasonal features, we used the whole match-ups dataset (more than 650 000 for OPEMW-RGN and more than 1 600 000 for OPEMW-RNC) and computed the monthly mean difference between ground-reference (either RGN or RNC) and OPEMW sri products. The results are shown in Fig. 12, where the error bars indicate the std of the monthly mean difference. Figure 12 shows that, with respect to RGN, OPEMW tends to underestimate sri from September to May, while the opposite in June, July, and August, though the monthly mean difference remains within $\pm 1\,\mathrm{mm\,h^{-1}}$. Conversely, with respect to RNC, OPEMW seems to overestimate sri throughout the year, with monthly mean difference within $-2\,\mathrm{mm\,h^{-1}}$. These results are likely influenced by the large amount of relatively low sri dominating the statistics (see Fig. 6), for which OPEMW agrees quite well with RGN but it is larger than RNC, as seen already in Figs. 7–9. As already anticipated, this feature is mainly related to the complex orography of the Italian territory. The std of the monthly mean difference does not seem to show an evident seasonal behaviour, with values between 2–4 $\mathrm{mm\,h^{-1}}$ (except for March 2012).

AMTD
6, 4279–4312, 2013

5 Summary and conclusions

One year of surface rain intensity (sri) data produced by the operational procedure OPEMW developed at IMAA-CNR has been validated against ground-based reference sri products from rain gauge (RGN) and weather radar (RNC) networks deployed over the Italian territory. The data set spans from July 2011 until June 2012, exploiting more than 3000 rain gauges and some 20 weather radars. Ground-based observations have been temporally and spatially colocated with the satellite observations, for a total of more than 650 000 OPEMW-RGN match-ups and more than 1 600 000 OPEMW-RNC match-ups. The distributions of sri from the three sources look quite similar, except that OPEMW shows more cases at smaller values (sri $\sim 1\,\mathrm{mm\,h^{-1}}$) and fewer cases at larger values (sri $\geq 15\,\mathrm{mm\,h^{-1}}$) relative to the other two.

The dichotomous statistical assessment showed 98 % accuracy in correctly identifying rainy and non-rainy FOVs (with respect to both RGN and RNC). The FB score is a bit larger than unity (with respect to both RGN and RNC), indicating that OPEMW has a tendency to slightly overestimate the precipitating areas. As a consequence, the FAR is rather high (64 %), while the POD is within 55–60 % (for RGN and RNC, respectively). Finally, HHS = 0.42–0.45 and ETS = 0.27–0.29 (the first number being with respect to RGN while the second to RNC), quantifying respectively the increase (with respect to random chance) in ability to detect rainy and non-rainy FOVS and rainy FOVs only. When dividing the dataset into seasons, all the dichotomous scores indicate that performances better than average are found in summer, fall, and spring, while significantly worse than average in the winter season. Low POD, HSS, and ETS values together with high FAR and FB values all seem to suggest that OPEMW tends to overestimate the precipitating areas during winter. These results, including the seasonal trend, are comparable with numbers found in Ebert et al. (2007), though those were obtained for 24 h accumulated rain. We also noted that for increasingly significant rainfall, the OPEMW detection skills become better and better (POD = 60–66 % and 83–88 % for detection limit set to 1 and $5\,\mathrm{mm\,h^{-1}}$, respectively).

AMTD
6, 4279–4312, 2013

The continuous statistical assessment, applied after "binning" the data set in the 0–15 mm h^{-1} range, shows a reasonably good correlation between OPEMW and RGN/RNC sri products; however, it is noticeable that OPEMW tends to slightly overestimate lower sri values, and conversely, to underestimate larger sri, with a sort of hinge point roughly around 6–7 mm h^{-1}. Up to 7 mm h^{-1} OPEMW is well correlated with the ground reference, specially with RGN, while the scatter increases significantly for sri > 10 mm h^{-1}, likely due to the low number of cases. Overall, the mean difference is within 0.8–2.8 mm h^{-1}, the std is within 2.6–3.1 mm h^{-1}, while the correlation is within 0.8–0.9. Better agreement (in terms of rms and correlation) is found with RNC rather than RGN, though this result is strongly influenced by the larger and statistically less significant sri values. The continuous statistical assessment does not show significant difference between the four seasons, all of which tend to confirm the results above. For low to moderate sri values (sri < 8 mm h^{-1}) we found that OPEMW overestimate RNC, but agrees well with RGN, suggesting a possible RNC sri underestimation primarily due to the complex Italian orography.

We also investigated the spatial and temporal behaviour of the mean absolute difference between OPEMW and ground-reference (either RGN or RNC) sri products. Two geographical-seasonal features are noticed: (i) increased mean absolute difference over the Alps and along the northern Apennines during winter, which we attribute to a residual spurious effect due to snow on the ground and (ii) larger mean absolute differences over Sicily than for the rest of Italy with respect to RGN, which we attribute to larger errors affecting the rain gauges deployed in Sicily rather than to inaccurate satellite estimates. Finally, the monthly mean difference between OPEMW and ground-reference sri products shows that OPEMW underestimates RGN from September to May, while the opposite in June, July, and August, with a monthly mean difference remaining within ±1 mm h^{-1}. Conversely, OPEMW seems to overestimate RNC throughout the year, with monthly mean difference within −2 mm h^{-1}. These results are likely influenced by the large amount of relatively low sri dominating the statistics, for which OPEMW agrees quite well with RGN but is larger than RNC, maybe due to the radar

AMTD
6, 4279–4312, 2013

attenuation issue mentioned above. The std of the monthly mean difference do not seem to show an evident seasonal behaviour, with values between 2–4 mm h^{-1}.

In conclusion, the validation effort presented here extends the PEMW validation presented by Di Tomaso et al. (2009) – which was limited to few case studies – to a full year of operational OPEMW products. The rain detection and estimation performances are confirmed. Sources of discrepancies with respect to ground-based references have been identified and discussed, and will be considered in the on-going work to improve the overall performances of OPEMW.

Appendix A

Definitions of statistical scores

This Appendix summarizes the statistical scores used for evaluating surface rain intensity (sri) estimated from satellite by OPEMW with respect to ground-based measurements from rain gauge (RGN) and weather radar (RNC) networks. These include the accuracy, the frequency bias score, the probability of detection (POD), the false alarm ratio (FAR), the Heidke skill score (HSS) and the equitable threat score (ETS). Equations for the above scores are taken from Ebert et al. (2007) and references therein. Every satellite-RGN (or satellite-RNC) match-up duplet, obtained as described in Sect. 3.1, can be classified as a hit (H, observed rain correctly detected), miss (M, observed rain not detected), false alarm (F, rain detected but not observed), or null (N, no rain observed nor detected) event. The sum $H + M + F + N$ is equal to the sample size S. The accuracy score is defined as $(H + N)/S$, and it indicates the fraction of total sample that has been correctly identified as rainy or non-rainy. The FB score is defined as $(H + F)/(H + M)$, and it is the ratio of the estimated to observed rain areas, thus indicating whether there is a tendency to over or underestimate the area subject to rain (bias score > 1 or < 1, respectively). The probability of detection, POD $= H/(H+M)$ gives the fraction of rain occurrences that were correctly detected, while the false alarm

AMTD
6, 4279–4312, 2013

ratio, FAR = $F/(H+F)$, measures the fraction of rain detections that were actually false alarms. By considering the number of hits that could be expected due purely to random chance, given by He = $(H+M)(H+F)/S$, the HSS score is defined as:

$$\mathrm{HSS} = (H + N - \mathrm{He})/(S - \mathrm{He})$$

indicating the fraction of correctly detected FOVs (as rainy or non-rainy) but after eliminating the fraction correctly identified due to random chance. Similarly to this, the ETS is defined as:

$$\mathrm{ETS} = (H - \mathrm{He})/(H + M + F - \mathrm{He})$$

indicating the fraction of correctly detected FOVs (as rainy), adjusted for the number of hits that could be expected due purely to random chance. ETS is more severe than HSS since it does not take into consideration the corrected negatives. The ETS is commonly used as an overall skill measure by the numerical weather prediction community, with accuracy, FB, POD, and FAR providing complementary information on bias, misses, and false alarms.

Acknowledgements. This work is partially funded by the Italian project IDRA (cetemps.aquila.infn.it/idra) commissioned by the Department of Civil Protection (DPC, www.protezionecivile.it) to CETEMPS, University of L'Aquila. Radar and rain gauge data have been provided by the DPC through the IDRA project. The authors are grateful to Klaide De Sanctis and Livio Bernardini of HIMET (www.himet.it) for helping with radar network data and the OPEMW output visualization, and to Graziano Giuliani for helping with the OPEMW implementation.

References

Anagnostou, E. N.: Overview of overland satellite rainfall estimation for hydro-meteorological applications, Surv. Geophys., 25, 511–537, 2004.

AMTD
6, 4279–4312, 2013

Antonelli, P., Puca, S., Zauli, F., Bennartz, R., de Leonibus, L., Feltz, W., and Woolf, H.: Validation of satellite rain rate estimation with ground-based observing systems, in: Integrated Ground-Based Observing Systems, edited by: Cimini, D., Marzano, F. S., and Visconti, G., doi:10.1007/978-3-642-12968-1_14, Springer-Verlag, Berlin, Heidelberg, 2010.

Bennartz, R.: Optimal convolution of AMSU-B to AMSU-A, J. Atmos. Ocean. Technol., 17, 1215–1225, doi:10.1175/1520-0426(2000)017¡1215:OCOABT¿2.0.CO;2, 2000.

Di Tomaso, E., Romano, F., and Cuomo, V.: Rainfall estimation from satellite passive microwave observations in the range 89 GHz to 190 GHz, J. Geophys. Res., 114, D18203, doi:10.1029/2009JD011746, 2009.

Kidd, C. and Levizzani, V.: Status of satellite precipitation retrievals, Hydrol. Earth Syst. Sci., 15, 1109–1116, doi:10.5194/hess-15-1109-2011, 2011.

Ebert, E., Janowiak, J. E., and Kidd, C.: Comparison of near-real-time precipitation estimates from satellite observations and numerical models, B. Am. Meteorol. Soc., 2007, 47–64, doi:10.1175/BAMS-88-1-47, 2007.

EUMETSAT: ATOVS Level 1b Product Guide, Ref.: EUM/OPS-EPS/MAN/04/0030, v3, Jan 2010, available at: http://oiswww.eumetsat.org/WEBOPS/eps-pg/ATOVS-L1/ATOVSL1-PG-index.htm (last access: 20 February 2013), 2010.

Kummerow, C.: Beam-filling errors in passive microwave rainfall retrievals, J. Appl. Meteorol., 37, 356–370, 1998.

Levizzani, V., Bauer, P., and Turk, F. J., eds.: Measuring Precipitation from Space – EURAINSAT and the Future, Dordrecht, The Netherlands, Springer, 748 pp., ISBN-10:1402058349, 2007.

Marshall, J. S. and Palmer, W. M.: The distribution of raindrops with size, J. Meteor., 5, 165–166, 1948.

Marzano, F. S., Vulpiani, G., and Picciotti, E.: Rain field and reflectivity vertical profile reconstruction from C-band radar volumetric data, IEEE Trans. Geosci. Remote, 42, 1033–1046, 2004.

Marzano, F. S., Ronzoni, M., Montopoli, M., Di Fabio, S., Picciotti, E., and Vulpiani, G.: Statistical characterization of C-band single-polarization radar retrieval space-time error in complex orography, Proc. of ERAD 2012 – The Seventh European Conference On Radar In Meteorology And Hydrology, Tolouse (France), 25–29 June 2012, QPE-244, 2012.

Montopoli, M., Marzano, F. S., Picciotti, E., and Vulpiani, G.: Spatially-adaptive advection radar technique for precipitation mosaic nowcasting, IEEE TGRS, 5, 874–884, doi:10.1109/JSTARS.2011.2182506, 2012.

AMTD
6, 4279–4312, 2013

NCDC/NOAA: NOAA KLM User's Guide Section 3.4, Dec. 2008, available at: http://www2.ncdc.noaa.gov/docs/klm/html/c3/sec3-4.htm (last access: 20 February 2013), 2008.

Nunes, A. M. B. and Roads, J. O.: Influence of precipitation assimilation on a regional climate model's surface water and energy budgets, J. Hydrometeor., 8, 642–664, 2007.

Ricciardelli, E., Romano, F., and Cuomo, V.: Physical and statistical approaches for cloud identification using MSG-SEVIRI data, Remote Sens. Environ., 112, 2741–2760, 2008.

Ricciardelli, E., Romano, F., Cimini, D., Marzano, F. S., and Cuomo, V.: A statistical approach for rainfall confidence estimation using MSG-SEVIRI observations, Proc. EUMETSAT Meteorological Satellite Conference, Cordoba 20–24 September, ISBN 978-92-9110-089-7, 2010.

Romano, F., Cimini, D., Rizzi, R., and Cuomo, V.: Multilayered cloud parameters retrievals from combined infrared and microwave satellite observations, J. Geophys. Res., 112, D08210, doi:10.1029/2006JD007745, 2007.

UK Met Office: AAPP Overview Document, NWPSAF-MO-UD-004, Version 7, http://research.metoffice.gov.uk/research/interproj/nwpsaf/aapp/NWPSAF-MO-UD-004_Overview.pdf (last access: 20 February 2013), 2011.

Vulpiani, G., Pagliara, P., Negri, M., Rossi, L., Gioia, A., Giordano, P., Alberoni, P. P., Cremonini, R., Ferraris, L., and Marzano, F. S.: The Italian radar network within the national early-warning system for multi-risks management, Proc. of Fifth European Conference on Radar in Meteorology and Hydrology, ERAD, 30 June–4 July 2008, Helsinki, Finnish Meteorological Institute, 184, 2008a.

Vulpiani, G., Tabary, P., Parent-du-Chatelet, J., and Marzano, F. S.: Comparison of advanced radar polarimetric techniques for operational attenuation correction at C band, J. Atmos. Oceanic Tech., 25, 1118–1135, doi:10.1175/2007JTECHA936.1, 2008b.

Vulpiani, G., Montopoli, M., Delli Passeri, L., Gioia, A. G., Giordano, P., and Marzano, F. S.: On the use of dual-polarized C-band radar for operational rainfall retrieval in mountainous areas, J. Appl. Meteor. Climatol., 51, 405–425, doi:10.1175/JAMC-D-10-05024.1, 2012.

AMTD
6, 4279–4312, 2013

Table 1. Results of the dichotomous statistical assessment for OPEMW sri product with respect to RGN and RNC products.

	RGN					RNC				
	Summ.	Fall	Wint.	Spri.	All	Summ.	Fall	Wint.	Spri.	All
Acc.	0.99	0.98	0.96	0.97	0.98	0.99	0.99	0.97	0.98	0.98
HSS	0.46	0.54	0.18	0.54	0.42	0.49	0.58	0.26	0.57	0.45
ETS	0.30	0.37	0.10	0.37	0.27	0.33	0.41	0.15	0.40	0.29
FB	1.99	0.97	3.44	1.08	1.54	1.73	1.29	2.81	1.08	1.10
POD	0.70	0.55	0.44	0.57	0.55	0.67	0.67	0.53	0.60	0.60
FAR	0.65	0.44	0.87	0.47	0.64	0.61	0.48	0.81	0.45	0.64

AMTD
6, 4279–4312, 2013

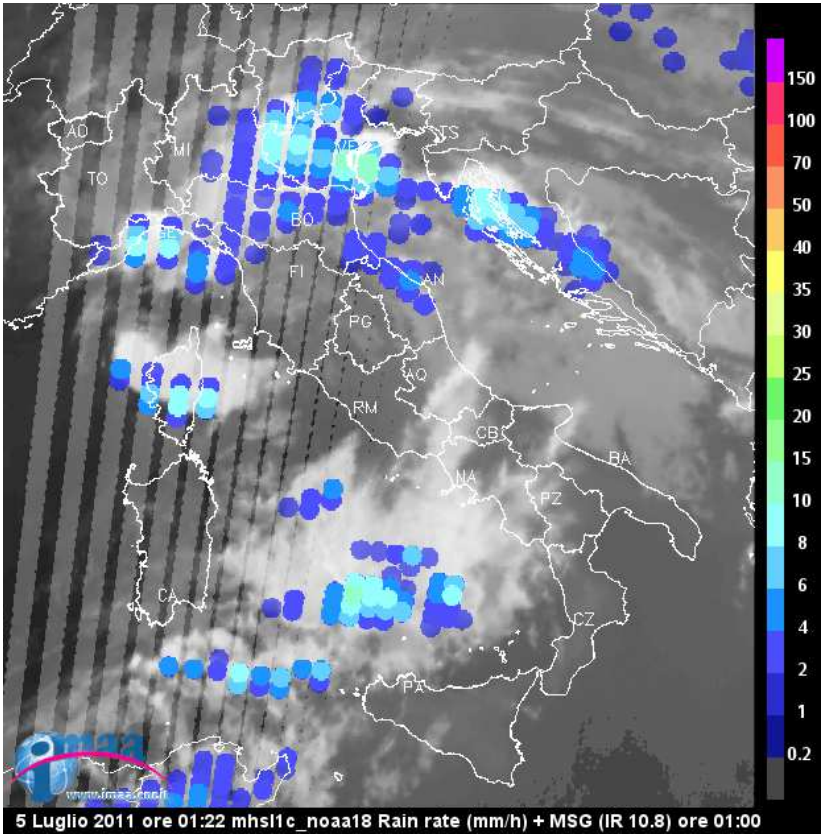

Fig. 1. An example of the graphical output of OPEMW (the MHS FOVs are represented as uniform circles along the scan line). The surface rain intensity (sri) product is color-coded according to the vertical bar (in mm h^{-1}) and layered over the Meteosat Second Generation (MSG) 10.8 µm image (in normalized inverted grey scale). Data obtained from MHS on NOAA N-18 overpass at 01:22 UTC and MSG observations at 01:00 UTC on 5 July 2011.

AMTD
6, 4279–4312, 2013

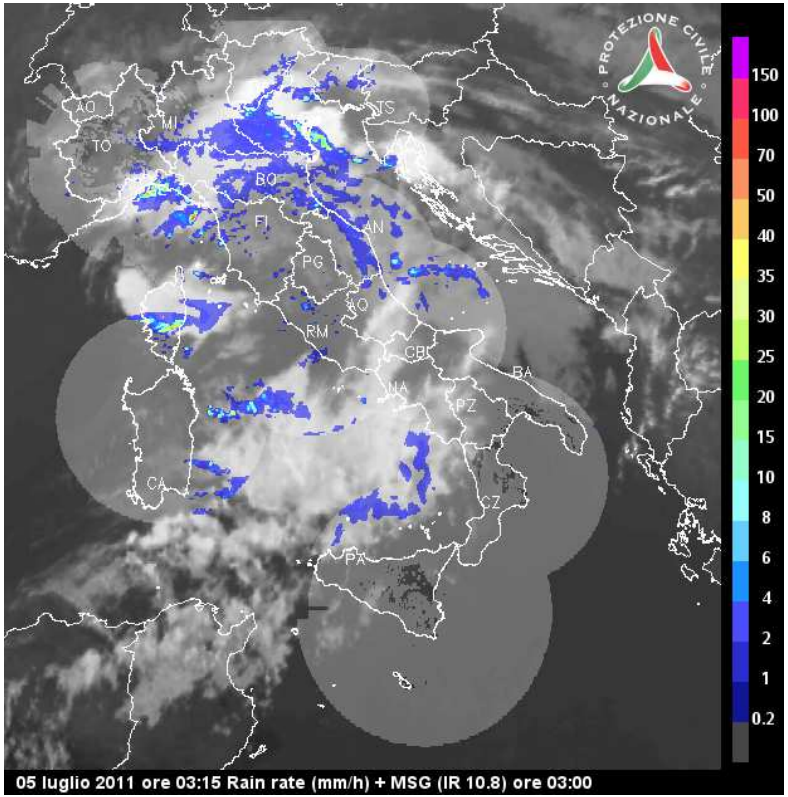

Fig. 2. An example of the graphical output of RNC (courtesy of DPC). The surface rain intensity (sri) product is color-coded according to the vertical bar (in mm h^{-1}) and layered over the Meteosat Second Generation (MSG) 10.8 µm image (in normalized inverted grey scale). Data obtained from RNC at 01:15 UTC and MSG observations at 01:00 UTC on 5 July 2011 (i.e. within 7 min from data in Fig. 1). Note that here the time displayed at the bottom is in CEST (Central Europe Summer Time).

AMTD
6, 4279–4312, 2013

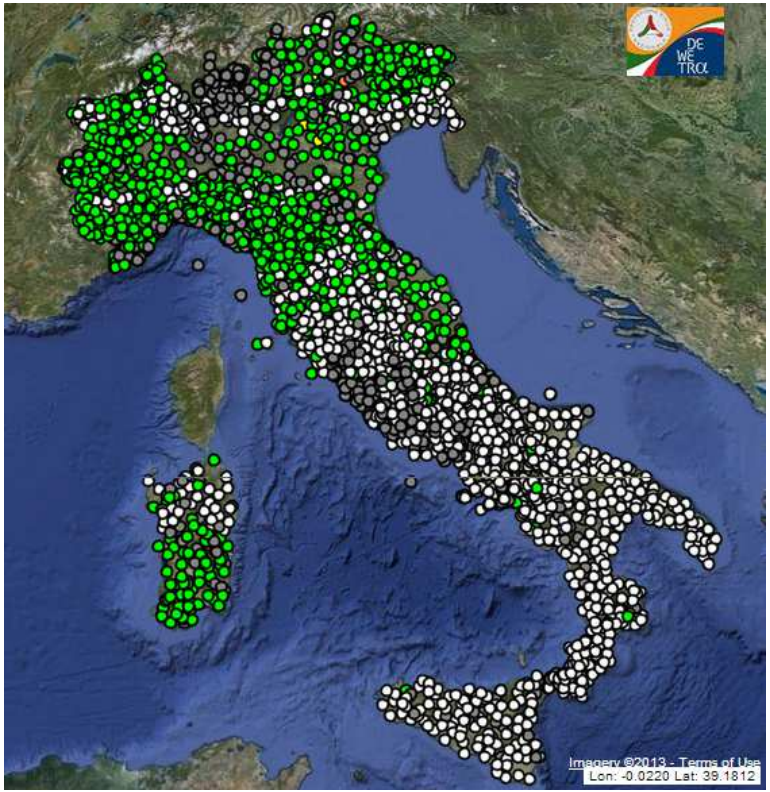

Fig. 3. The distribution of more than 3000 rain gauges over Italy. The figure shows 1 h accumulated rain (sri) between 01:00 and 02:00 UTC, on 5 July 2011 (i.e. the 1 h period containing both Figs. 1 and 2). Rain gauges are indicated with circles and color coded as follows: grey → missing data; white → no rain; green → 0 < sri < T1, yellow → T1 < sri < T2, orange → T2 < sri < T3; red → T3 < sri, where T*i* (with *i* = 1–3) represent three thresholds for light, moderate, and intense rainfall, which values differ depending on respective catchment (data courtesy of DPC. Image obtained using DEWETRA).

AMTD
6, 4279–4312, 2013

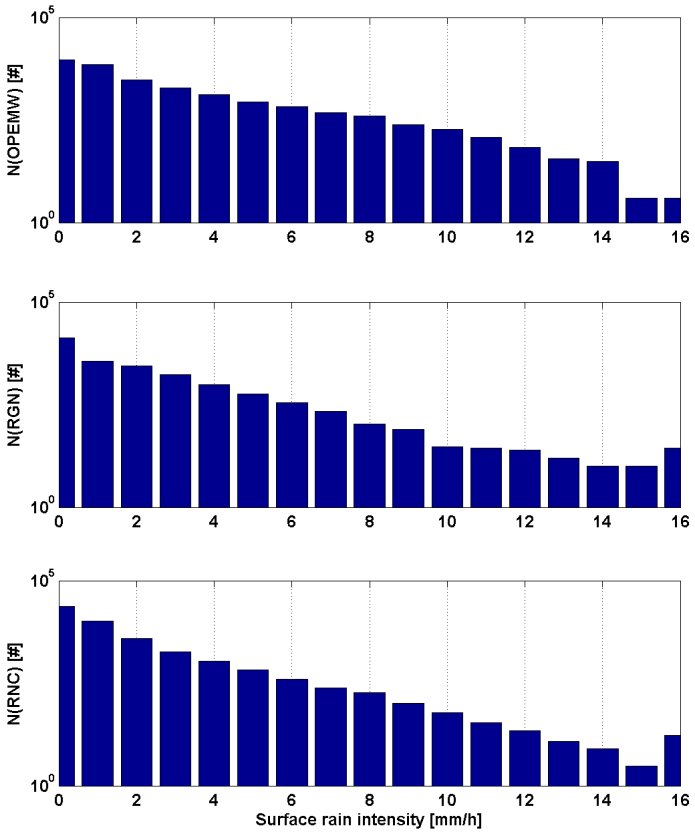

Fig. 4. Histograms of OPEMW (top), RGN (middle), and RNC (bottom) surface rain intensity (sri) products (vertical axis in log scale). Values greater than 15 mm h^{-1} are grouped in the last bin.

AMTD
6, 4279–4312, 2013

Validation of satellite OPEMW precipitation product

D. Cimini et al.

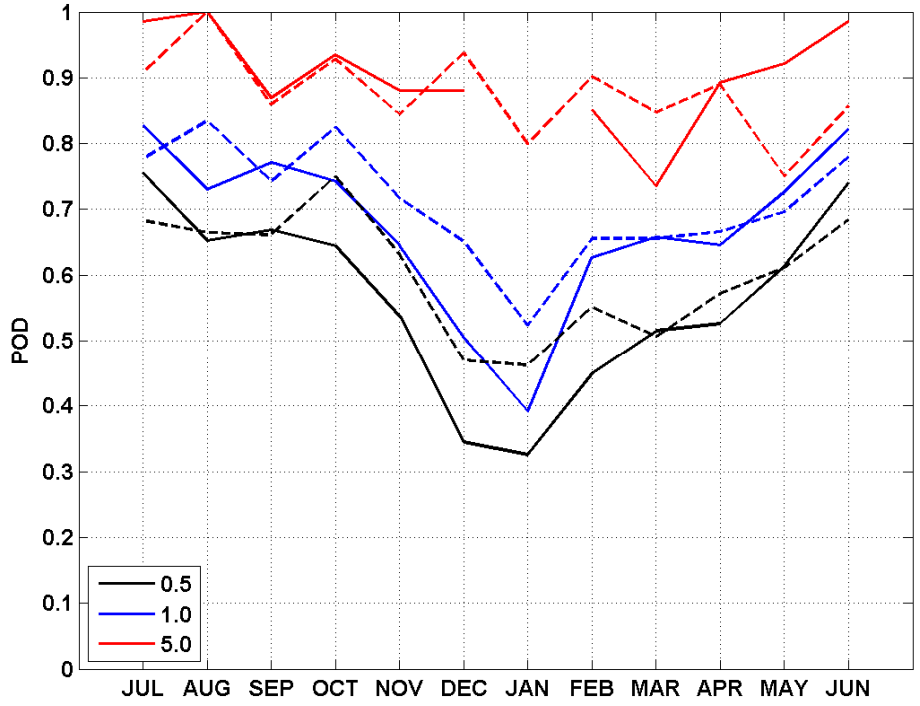

Fig. 5. Monthly POD as computed using three detection thresholds: 0.5 (black), 1.0 (blue), and 5.0 (red) mm h^{-1}. Solid and dashed lines indicate OPEMW results as compared with RGN and RNC, respectively. The value for RGN at 5 mm h^{-1} threshold is missing in January due to insufficient data points.

AMTD
6, 4279–4312, 2013

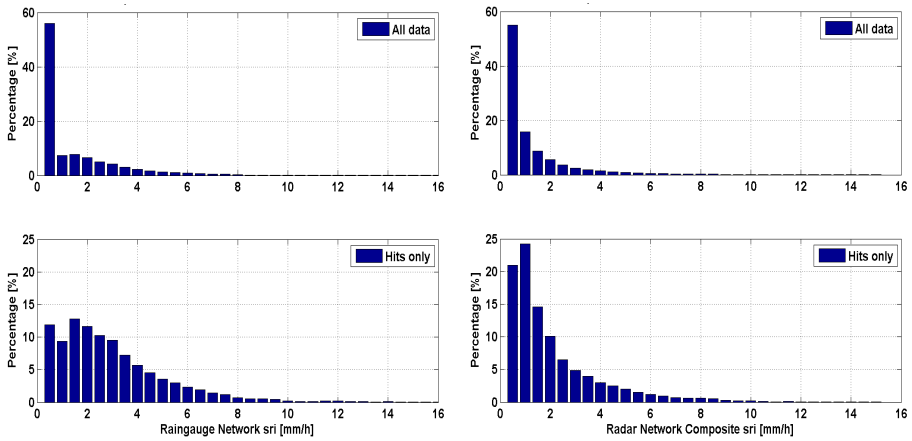

Fig. 6. Percentage histograms of binned analysis for OPEMW sri against RGN (left) and RNC (right) sri products. All match-up data are included in the upper panels, while hits-only data are shown on bottom panels.

AMTD
6, 4279–4312, 2013

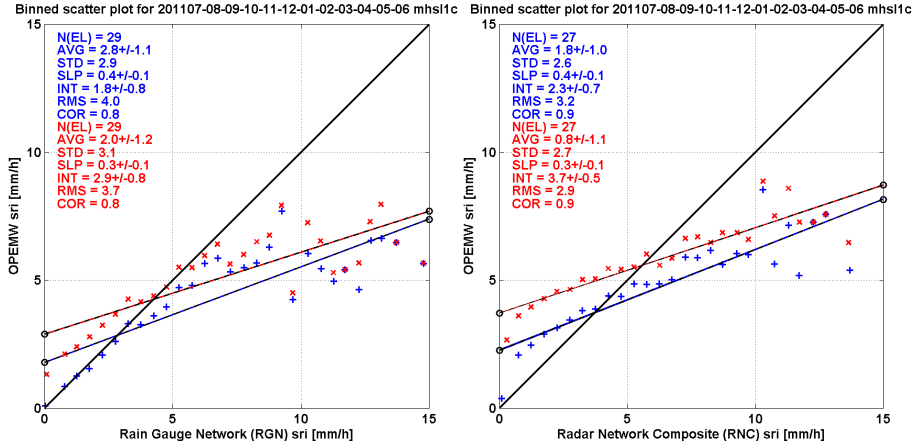

Fig. 7. Scatter plot of binned analysis for the 1 yr period under analysis (July 2011–June 2012). y-axis report the OPEMW sri product, while x-axis report RGN sri (left) and RNC sri (right) products. Blue markers indicate results using all data, while red crosses indicate results considering hits only. Main statistics are shown, as the number of available bins (*N*), the mean (AVG), standard deviation (STD), and root-mean squared (RMS) difference, the correlation coefficient (COR), and the slope (SLP) and intercept (INT) for a linear fit. Numbers after the ± sign indicate the 95 % confidence interval.

AMTD
6, 4279–4312, 2013

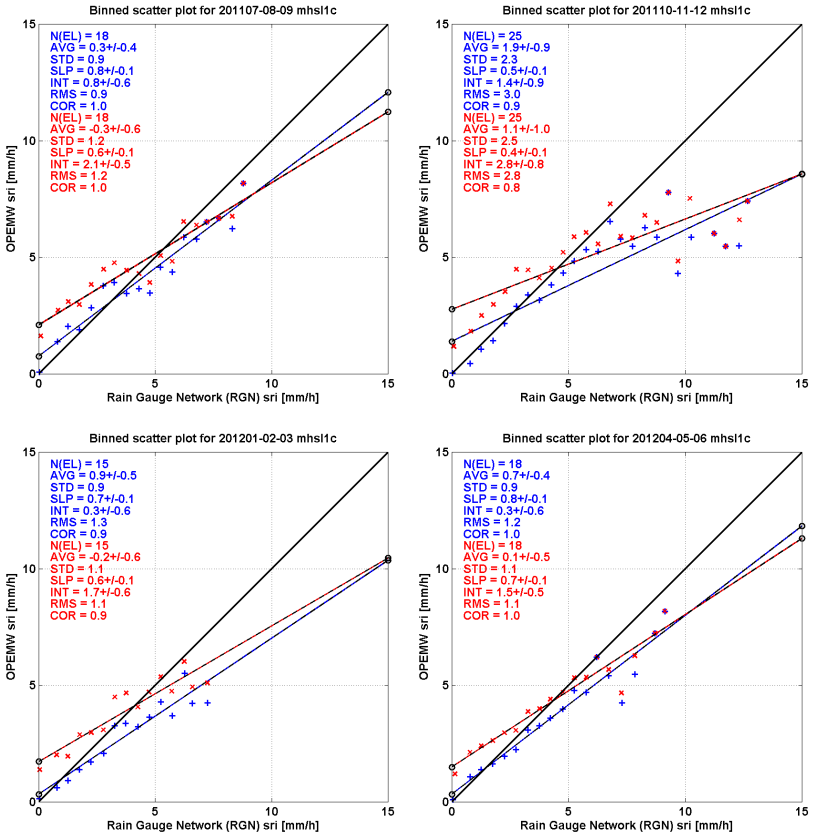

Fig. 8. Scatter plot of seasonal binned analysis with respect to RGN; clockwise from top-left panel: Summer (July-August-September 2011), Fall (October-November-December 2011), Winter (January-February-March 2012), and Spring (April-May-June 2012). Markers and statistics are as in Fig. 7.

AMTD
6, 4279–4312, 2013

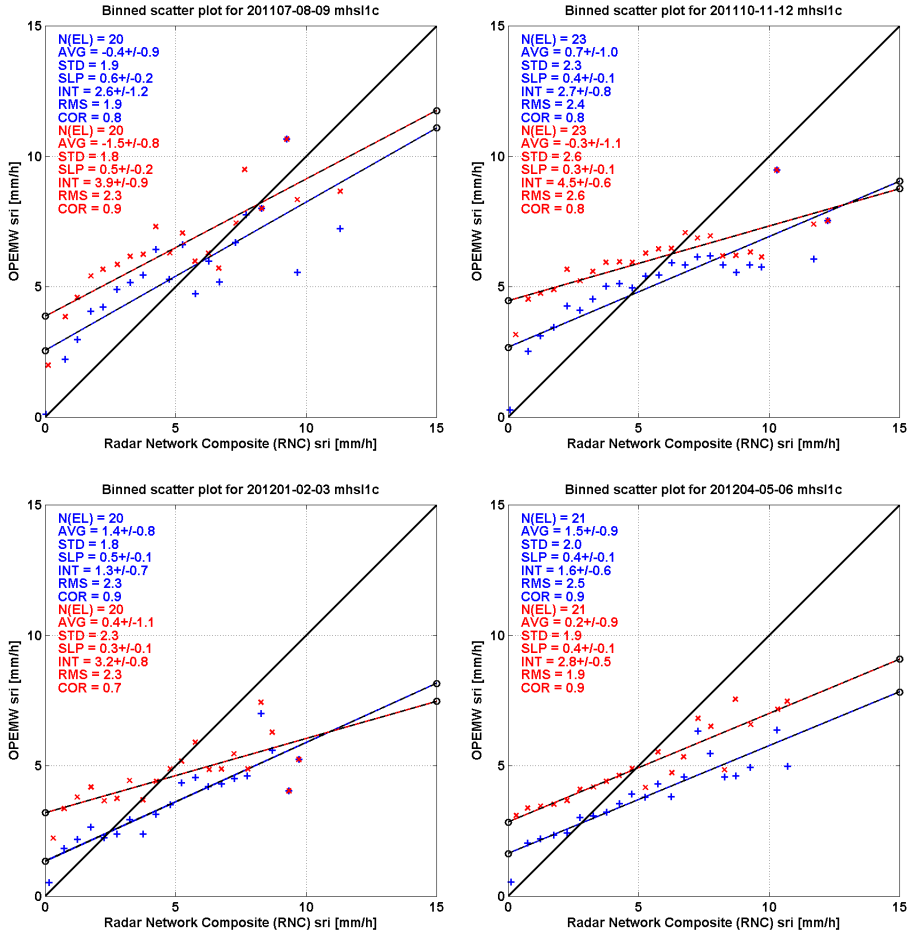

Fig. 9. Scatter plot of seasonal binned analysis as in Fig. 8, but with respect to RNC. Clockwise from top-left panel: Summer, Fall, Winter, and Spring. Markers and statistics are as in Fig. 7.

AMTD
6, 4279–4312, 2013

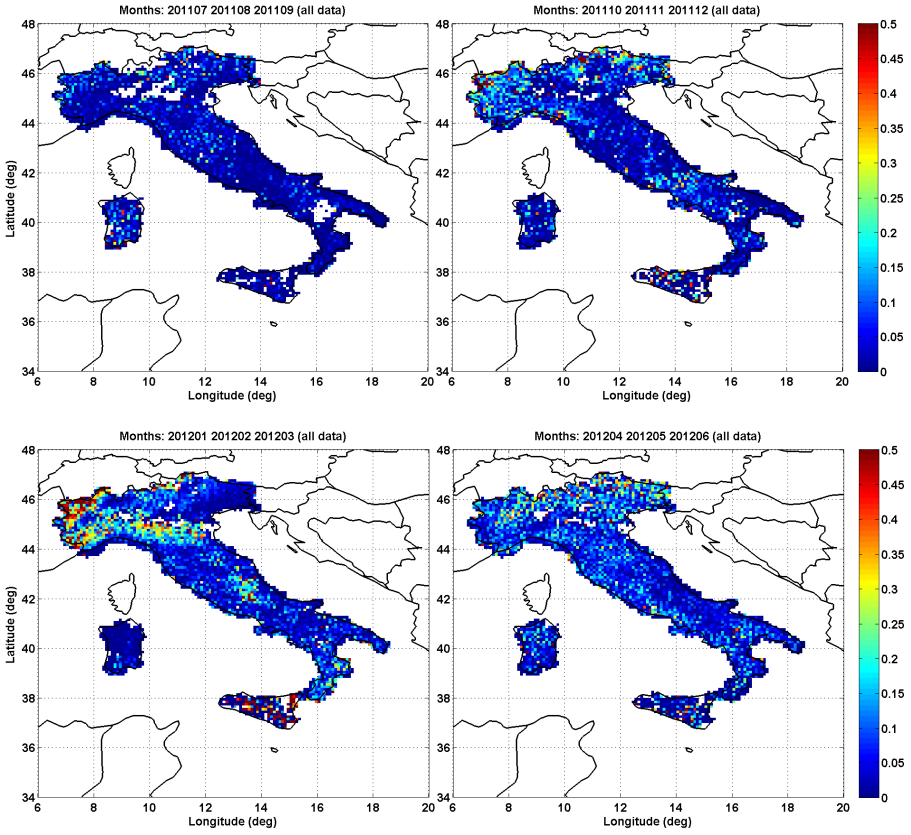

Fig. 10. Maps of seasonal mean absolute difference with respect to RGN; clockwise from top-left panel: Summer (July-August-September 2011), Fall (October-November-December 2011), Winter (January-February-March 2012), and Spring (April-May-June 2012). The vertical color bar is in mm h^{-1}.

AMTD
6, 4279–4312, 2013

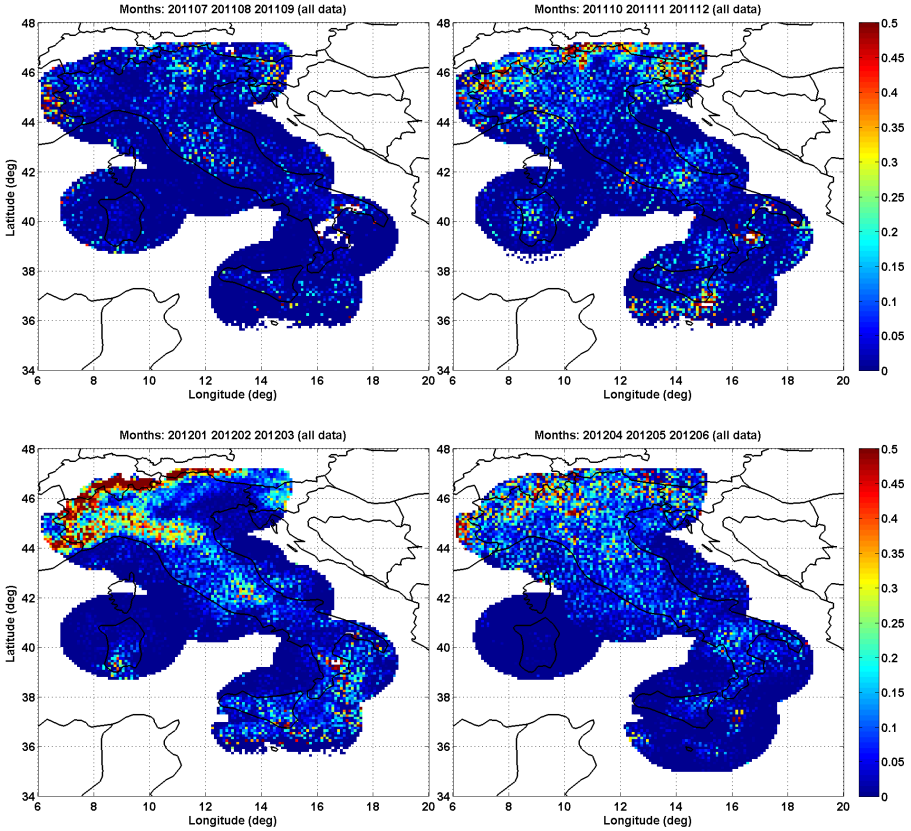

Fig. 11. As in Fig. 7 but with respect to RNC. Clockwise from top-left panel: Summer, Fall, Winter, and Spring. The vertical color bar is in mm h^{-1}.

AMTD
6, 4279–4312, 2013

Validation of satellite OPEMW precipitation product

D. Cimini et al.

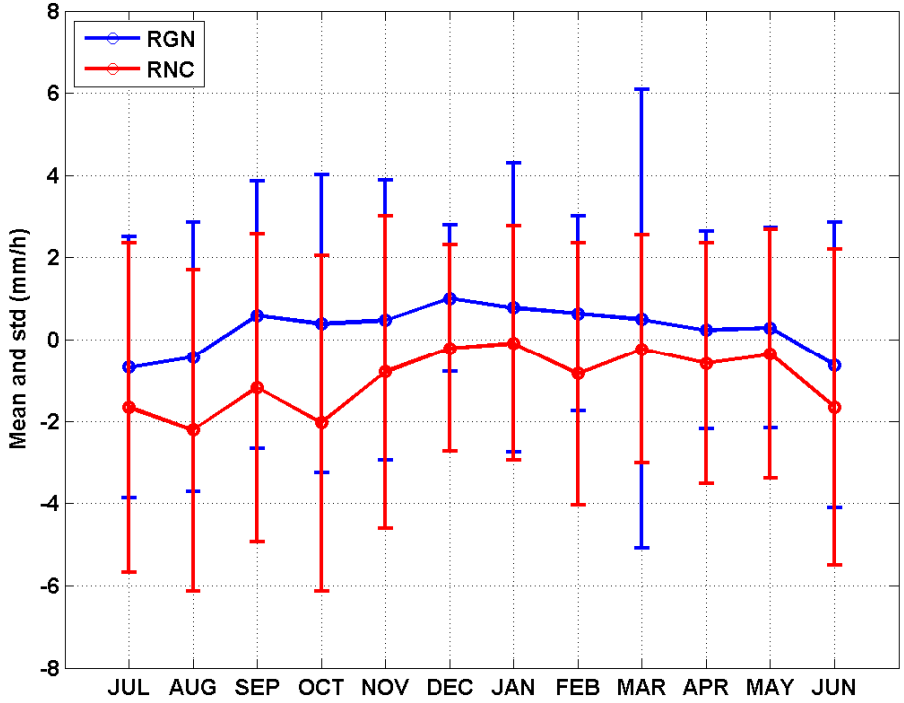

Fig. 12. Monthly mean difference (circles) and its standard deviation (error bars) of OPEMW sri product with respect to RGN (blue) and RNC (red) products. Mean difference is computed as RGN (or RNC) minus OPEMW.

AMTD
6, 4279–4312, 2013